Corrosion Science 153 (2019) 74–84

Contents lists available at ScienceDirect

Corrosion Science

journal homepage: www.elsevier.com/locate/corsci

Corrosion onset associated with the reinforcement and secondary phases in B_4C-6061Al neutron absorber material in H_3BO_3 solution

Y.T. Zhou[a], Y.N. Zan[a], X.X. Wei[a], B. Yang[a], B. Zhang[a], S.J. Zheng[a], X.H. Shao[a], J.H. Dong[b], X.L. Ma[a,*], B.L. Xiao[a], Q.Z. Wang[c,*], Z.Y. Ma[a]

[a] Shenyang National Laboratory for Materials Science, Institute of Metal Research, Chinese Academy of Sciences, 72 Wenhua Road, Shenyang 110016, China
[b] Environmental Corrosion Centre, Institute of Metal Research, Chinese Academy of Sciences, 62 Wencui Road, Shenyang 110016, China
[c] Key Laboratory of Nuclear Materials and Safety Assessment, Institute of Metal Research, Chinese Academy of Sciences, 72 Wenhua Road, Shenyang 110016, China

ARTICLE INFO

Keywords:
A. Metal matrix composites
A. Aluminium
B. TEM
C. Pitting corrosion
C. Interfaces

ABSTRACT

The microstructures in B_4C-6061Al composite hot-pressed at different temperatures (560 °C, 620 °C) are characterized, and the corrosion behavior of the materials is studied using electrochemical tests and quasi in-situ TEM observations. The composite fabricated at 620 °C is composed of more matrix-reinforcement reaction products (Al_3BC at the interfaces and MgB_2 in the alloy matrix). Corrosion occurred slightly in boric acid but severely in Cl^--containing solution. The B_4C/Al interface in both samples is preferentially attacked and the MgB_2 dispersions in the high-temperature-pressed composite remarkably promoted the pitting. Dealloying of Mg_2Si precipitate does not obviously deteriorate the corrosion resistance of the composite.

1. Introduction

Owing to the light weight, high stiffness, as well as the superior thermal conductivity, B_4C particulate-reinforced aluminum matrix composite (AMC) has received considerable attentions in the past decades [1–3]. In the nuclear industry, this composite has been increasingly used as an ideal neutron absorber material in these years because of the high abundance of B^{10} isotope in B_4C and the good formability for extrusion and rolling [4–10].

For wet storage method, the spent nuclear fuels are enclosed by B_4C-Al composite plates and positioned in a pool filled with boric acid solution (2500-ppm boron). To minimize the service risk, the stability and corrosion mechanisms of the materials should be fully concerned. In the previous investigations, electrochemical analyses have been systematically carried out [11–21]. The composites showed good corrosion resistance in dilute H_3BO_3 solution but susceptible to pitting in Cl^--containing environment [16].

Generally, the corrosion rate of B_4C-Al composites is enhanced with increasing reinforcement contents. Galvanic coupling between reinforcement and matrix is of primary concern in most AMCs. Electrochemical tests indicated that B_4C particles could serve as cathodic sites in B_4C-Al system although it induced a rather low galvanic current [19]. Besides the galvanic effect, the discontinuity of oxide film at the B_4C/Al interfaces could decrease the corrosion resistance of the material as well [15]. Preferential corrosion in the vicinity of B_4C particles were ascribed to the above reasons [14,16,17].

Secondary phases in AMCs are another cause for the onset of localized corrosion. Li et al. have observed that the localized corrosion in a B_4C-6061Al composite occurred near the Si-rich precipitates [14]. Besides the commonly seen intermetallic precipitates in Al alloys, the products generated by the matrix-reinforcement reactions (MRR) are worth noting. For instance, Al_4C_3 as a reaction product is usually found in SiC-Al composites. Exposed to moisture, this compound is prone to hydrolyze, leading to the pitting and crevice corrosion of the composite [22]. Another example is the interface corrosion in boron fibers reinforced AMC. Pohlman et al. [23] demonstrated that the aluminum boride intermetallic which was the interfacial reaction products generated galvanic corrosion with the aluminum matrix and induced the corrosion attack of the composite. In the presently studied B_4C-Al system, B_4C particles are very reactive with liquid aluminum and some other alloying element, such as Mg, Ti, Zr etc. [24–26]. Considering the benefits to improve the mechanical property, a certain amount of interfacial reaction layers is actually preferred in the composite [27,28]. Therefore, the electrochemical effects of the reaction products should be paid more attentions. To our knowledge, however, the reaction products in the materials and how they exactly work in the corrosion process are far from known.

The insufficient understanding is largely attributed to the difficulty

* Corresponding authors.
E-mail addresses: xlma@imr.ac.cn (X.L. Ma), qzhwang@imr.ac.cn (Q.Z. Wang).

https://doi.org/10.1016/j.corsci.2019.03.042
Received 5 November 2018; Received in revised form 27 February 2019; Accepted 24 March 2019
Available online 27 March 2019
0010-938X/

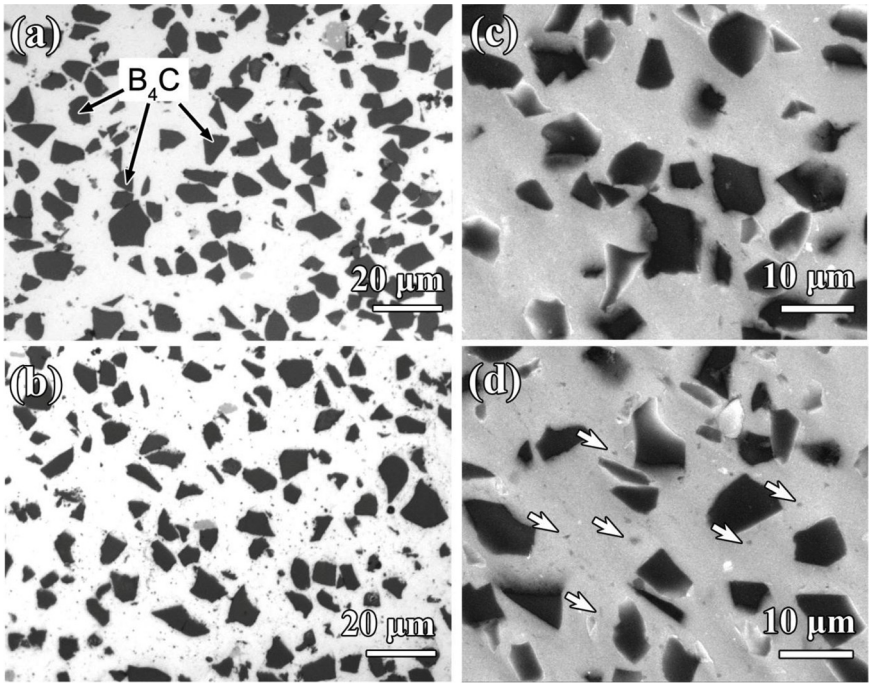

Fig. 1. Microstructures in B_4C-6061Al composite. (a) and (b) Optical micrographs of the samples HP560 and HP620, respectively. (c) and (d) SEM images of the samples HP560 and HP620, respectively. As arrowed in (d), nano-scale secondary phases are seen in the aluminum matrix in the sample HP620.

in establishing direct connections between the nanoscale microstructures and their corrosion behavior. The previous studies were mostly performed using electrochemical tests combined with scanning electron microscope (SEM) or optical microscope characterizations. Obviously, the characterization techniques could not fully disclose the B_4C/Al interfacial characteristics and the secondary phases in the composite. Besides, the observed corrosion sites were severely attacked, which made it hard to precisely trace the corrosion origin. Considering the length scale, transmission electron microscopy (TEM) seems suitable for the investigation. In recent years, quasi in-situ TEM experimental methods were developed for the corrosion research at nanoscale [29–31]. The present authors have also applied such technique to unravel the microstructural factors and compositional evolutions correlated with the pitting corrosion in several engineering alloys [32–35].

In this work, corrosion tests combined with quasi in-situ TEM investigations were performed to study the corrosion onset on B_4C-6061Al neutron absorber material, trying to clarify the microstructural factors and their electrochemical roles to the degradation of the composite. This research is believed to provide fundamental knowledge for the materials design and fabrication.

2. Materials and experimental methods

2.1. Sample preparation

B_4C-6061Al composites were fabricated by powder metallurgy (PM) technique. 6061Al alloy with a nominal composition of Al-1.0Mg-0.65Si (wt.%) and 21 wt.% B_4C particles with diameter of about 7 μm were used to fabricate the composite. The purity of B_4C particles was 96.5 pct. Through XRD analysis, the main impurities in B_4C were free B, C and B_2O_3.

The as-mixed Al and B_4C powders were cold-pressed in a cylindrical die under a pressure of 50 MPa and then hot-pressed under a pressure of 30 MPa for 2 h, producing the composite billets. The hot-pressing temperature was set as 560 °C and 620 °C to control the chemical reaction between B_4C and aluminum matrix (The samples were named after HP560 and HP620, respectively, in the following for short). The billets were hot-forged at 480 °C and then hot-rolled at 450 °C into sheets with 2 mm in thickness.

2.2. Microstructural characterization

The microstructures were characterized by Hitachi SU-70 scanning electron microscope (SEM) and an FEI Tecnai G2 F30 transmission electron microscope, equipped with a high-angle-angular-dark-field (HAADF) detector and X-ray energy-dispersive spectrometer (EDS) systems. In the experiments, HAADF-STEM imaging was mainly used since the contrast in this mode is sensitive to the local compositions and the specimen thickness [36].

TEM samples were sliced from the B_4C-6061Al plates by a linear precision saw. The specimen discs with a diameter of 3 mm were ground using silicon carbide papers, dimpled to 1 μm finish, and finally thinned by ion-milling system Gatan PIPS 695.

2.3. Electrochemical testing

The composite samples used for electrochemical tests and immersion tests were cut into 1 cm × 1 cm slices, then ground using various grit silicon carbide papers and polished with diamond paste to 5 μm finish. In the electrochemical tests, a traditional three-electrode system was used: the B_4C-6061Al composite as the working electrode, a platinum foil as the counter electrode and a saturated calomel electrode (SCE) as the reference electrode. The tested solutions, H_3BO_3 solution at 2500-ppm boron (pH ≈ 4.9) and the same H_3BO_3 solution with addition of NaCl (600-ppm Cl), were not deaerated and maintained at room temperature. AUTOLAB PGSTAT302 N electrochemical workstation was used in potentiodynamic polarization measurements. The experimental parameters were the following: 120 s delay at open circuit (oc) prior to the polarization tests, potentiodynamic scan started at 250 mV below V_{OC}. The potential scan rate used was 0.33 mV/s.

Quasi in-situ TEM observations were carried out following the procedures: after the first-round TEM observations, the TEM specimen was taken out and then immersed into solution at room temperature for various periods. To increase the corrosion rate, H_3BO_3 (2500-ppm

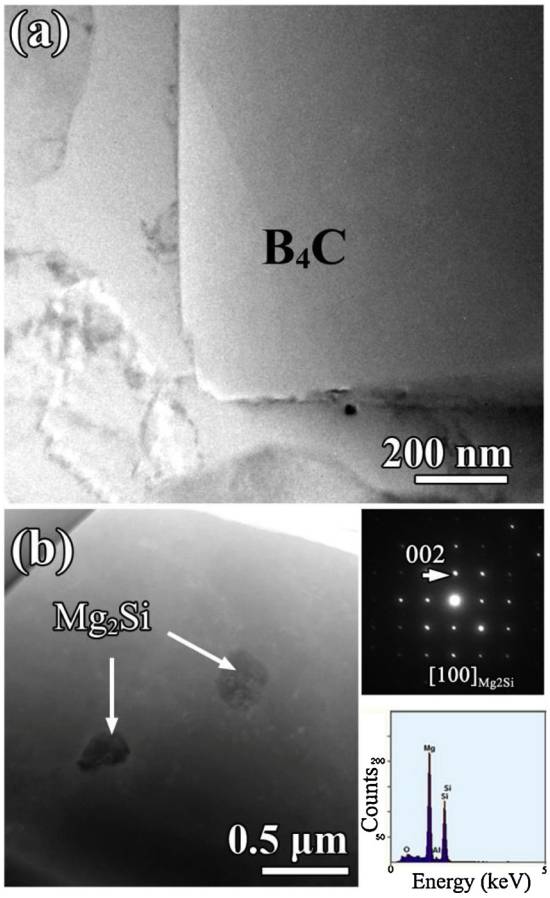

Fig. 2. TEM characterizations of the sample HP560. (a) Bright-field (BF) TEM image of a B_4C/Al interface. Interfacial reaction product was not observed at the interface. (b) A HAADF image showing the Mg_2Si precipitates in the alloy matrix. Electron diffraction pattern and the EDS profile of Mg_2Si precipitate are also given.

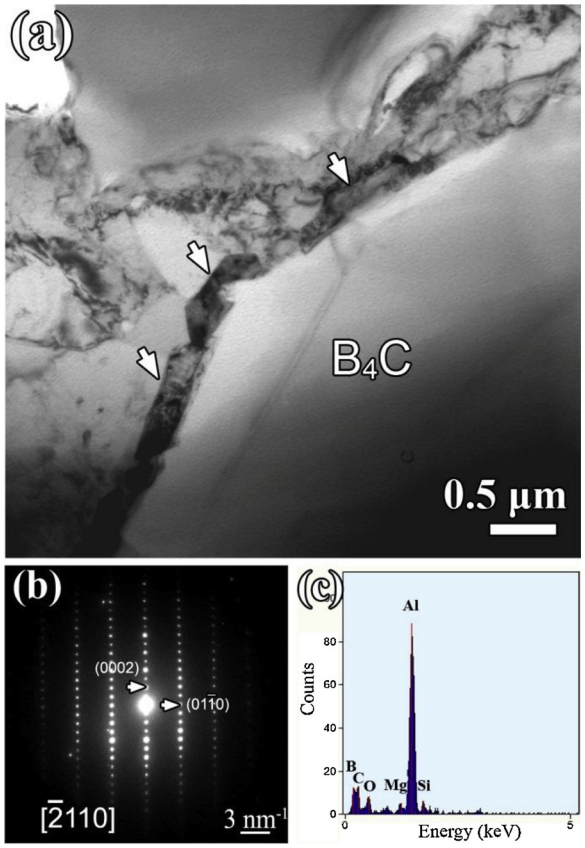

Fig. 3. TEM characterizations of the B_4C/Al interface in the sample HP620. (a) BF-TEM image showing the reaction product Al_3BC at the interface. (b) and (c) are the electron diffraction pattern and EDS profile of the Al_3BC compound.

boron) + NaCl (600-ppm chloride) solution was chosen for the quasi in-situ TEM experiments. After immersion, the corroded specimens were cleaned by distilled water, dried, and then moved to TEM for the second-round investigations.

3. Results

3.1. Microstructures in B_4C-6061Al composites

Optical micrographs of the as-rolled composites HP560 and HP620 are respectively shown in Fig. 1(a) and (b) in which the microstructures of the two composites are directly compared. The dark particles are B_4C reinforcements which were uniformly distributed. The samples were then characterized by high-magnification SEM. The images in Fig. 1(c) and (d) give more details. No macro-crevice was observed at the B_4C/Al interfaces. In addition, a high density of tiny phases (some of them were marked by arrows) appeared in aluminum matrix in the sample HP620, whereas the matrix in the sample HP560 was relatively 'clean'.

To identify the secondary phases in the samples, TEM characterizations were carried out. Fig. 2(a) is a bright-field TEM (BF-TEM) image of a B_4C/Al interface in the sample HP560. The sharp interphase boundary indicates it is free of interfacial reaction. In the alloy matrix, Mg and Si containing precipitates were frequently seen. Fig. 2(b) is a HAADF micrograph of the precipitates in the matrix. The corresponding SAED pattern and the EDS profile are shown on the right side. The SAED pattern can be well indexed as an fcc lattice (lattice constant a = 0.45 nm) along the [100] zone axis. Combining the diffraction information and chemical compositions suggested that the precipitates are β-Mg_2Si which is a typical precipitate in 6xxx series alloys.

Compared to the sample HP560, the microstructures were remarkably changed in the composite HP620. As displayed in the BF-TEM image in Fig. 3(a), discrete nanoparticles appeared at the B_4C/Al interface, suggesting the MRR at the interface. The thickness of the reaction product layer was measured to be ~300 nm. Electron diffraction (Fig. 3(b)) and EDS analysis (Fig. 3(c)) performed on these nanoparticles suggested they were Al_3BC phase (a = 0.349 nm, c = 1.154 nm, space group $P6_3/mmc$).

As illustrated in the SEM image in Fig. 1(d), the reaction products were present in the aluminum matrix as well. The TEM image of the dispersive phase is shown in Fig. 4(a). As marked by white arrows, several nano-rods located either at grain boundaries or in the grains. Fig. 4(b) gives the electron diffraction pattern. The EDS profile in Fig. 4(c) were obtained from a nano-rod located at the very edge of the peroration in TEM foil in order to avoid the signal from aluminum matrix. It indicates the compound mainly composed of Mg, Al and B. The diffraction and composition information confirmed these nano-rods being $Mg(Al)B_2$ compound (it is named after MgB_2 for short) which has the same crystalline structure as MgB_2 or AlB_2. Their sizes ranged from several ten nanometers to several micrometers. Besides Al_3BC and MgB_2 compounds, we did not find other reaction products in our massive TEM observations. Moreover, Mg_2Si precipitates were also rarely found in this specimen.

Alloying elements Mg and Si in 6xxx Al alloys are usually present in the form of Mg-Si phases or Al-Mg-Si-Cu phases depending on the Cu content in alloys. When the B_4C-Al composite was heated to above 600 °C, liquid aluminum appeared and facilitated the MRR occurring [37]. First reaction took place at the interfaces between B_4C and aluminum, yielding Al_3BC and free boron. Then the latter easily diffused

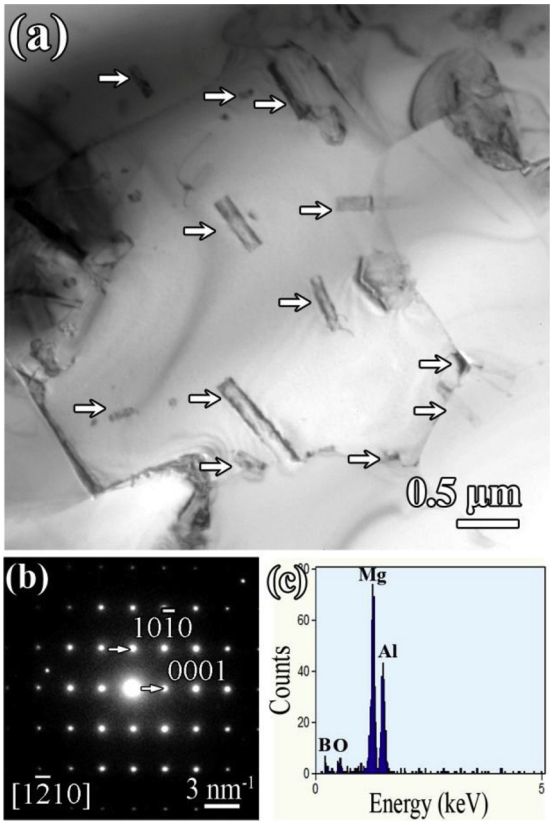

Fig. 4. Nano-scale reaction products in the sample HP620. (a) BF-TEM image showing the nano-rods dispersed in the alloy matrix. (b) Electron diffraction pattern and (c) EDS profile of the nano-rod, suggesting that the nano-rod is Mg(Al)B_2 or MgB_2 for short.

into the matrix through liquid phase network and combined alloying magnesium, producing dispersive MgB_2 nano-rods in the final composite. The combination of the two elements was attributed to the large electronegativity difference between them and resulted in the consumption of Mg_2Si precipitates. The MRR route can be written as follows: $3Al + B_4C \rightarrow Al_3BC + 3B$, and $2B + Mg \rightarrow MgB_2$

Our TEM characterization also indicated that a very small amount of MgB_2 nano-rods existed in the sample HP560, but Al_3BC were hardly seen. The MgB_2 dispersions in this sample were produced via the reaction between alloying Mg and the impurity boron or B_2O_3 in raw B_4C powders.

3.2. Corrosion susceptibility and initiations in the composites

To evaluate the corrosion resistance of the composites, potentiodynamic polarization tests on the above two samples were performed in H_3BO_3 electrolyte (2500-ppm boron). At least three specimens per condition were measured to ensure the accuracy of tests. The typical polarization curves are displayed in Fig. 5. For the two measured composites, the curve shapes are almost the same. Steep rises in the current were observed at the corrosion potential, suggesting pitting corrosion occurring on both specimens. Nevertheless, we could still find the difference in between. The anodic current density for the sample HP620 is one order of magnitude higher than that for HP560. Besides, a negative shift of nearly 100 mV of the corrosion potential E_{corro} for the HP620 is observed. The tests suggest that the corrosion susceptibility of the composite HP620 is remarkably higher.

Potentiodynamic polarization tests were also performed in the H_3BO_3 solution with addition of 600-ppm Cl^-. In the presence of Cl^-, both the samples underwent severe corrosion attack. From the anodic branches of the polarization curves, it is observed that the anodic

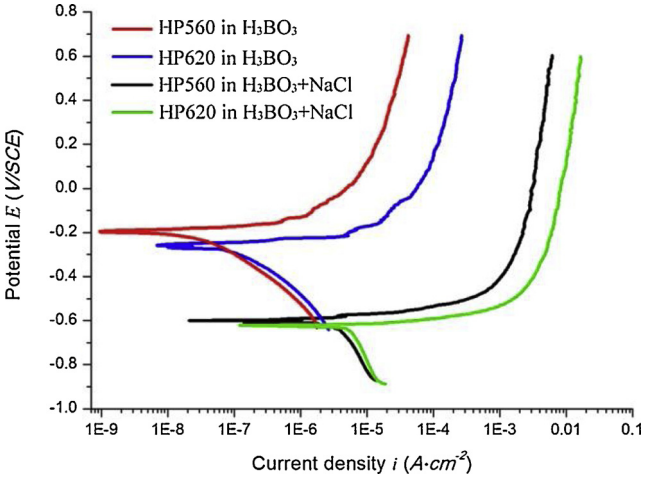

Fig. 5. Potentiodynamic polarization curves of the samples HP560 (red) and HP620 (blue) measured in H_3BO_3 solution. Black and green ones are the polarization curves of the HP560 and HP620 measured in H_3BO_3 solution with addition of 600-ppm Cl^-. (For interpretation of the references to colour in this figure legend, the reader is referred to the web version of this article.)

current density sharply increases to near 10 mA/cm^2. The comparatively higher current density for the sample HP620 also suggests the higher corrosion rate.

The different corrosion behavior of the composites was investigated by immersion tests in electrolytes as well. First tests were carried out in boric acid (2500-ppm boron). Fig. 6(a) and (b) are SEM images of the sample HP560 and HP620, respectively, experiencing immersion for 120 h. Corrosion product sedimentation fully covered both the sample surfaces. EDS analysis indicated that the sedimentation were mainly composed of Al and O. The corrosion product on the sample HP620 was much thicker, implying the higher corrosion rate. To reveal the corrosion initiations, the samples were characterized after removing the corrosion products. Fig. 6(c) shows the corrosion morphology on the sample HP560. Corrosion mostly happened at the B_4C/Al interfaces, as labeled by arrows. In comparison with the HP560, the HP620 corroded more severely. The corrosion pits were found not only at the B_4C/Al interfaces but also in the aluminum matrix. Obviously, the B_4C/Al interfaces in both samples showed high corrosion sensitivity, whereas the precipitate dispersions in the aluminum matrix also contributed to the high corrosion rate of the sample HP620.

In the presence of Cl^- in the solution, the materials corroded quite fast. The corrosion pits on the surfaces of samples HP560 and HP620 suffered only 24 h immersion were clearly visible under optical microscope. The Fig. 7(a) and (b) show the micrographs in which the pitting sites are marked by arrows. In comparison, the pits on the sample HP620 possess larger sizes. The corrosion sites on the samples HP560 and HP620 were further examined by SEM, as shown in Fig. 7(c) and (d), respectively. Similar to the corrosion morphology in the H_3BO_3 solution, corrosion trenches were often observed surrounding the B_4C reinforcements on the two samples, but deeper. Small pits were prevalent on the alloy matrix in the sample HP620 (Fig. 7(d)), but only a very small portion of the pits appeared on the HP560 (Fig. 7(c)).

To get a deep insight into the electrochemical roles played by the B_4C reinforcement and the nanoscale phases, we then carried out the quasi in-situ TEM observations. The experiments were operated in Cl^--containing H_3BO_3 solution.

Fig. 8(a) and (b) show the interface area in the specimen HP560 before and after immersion in electrolyte. In the latter image, a pit appears at the B_4C/Al interface. The pitting initiated at the corner of a notch on the B_4C surface. Taking a look at the site before corrosion (Fig. 8(a)), we did not find any evident crevice or secondary phase nearby.

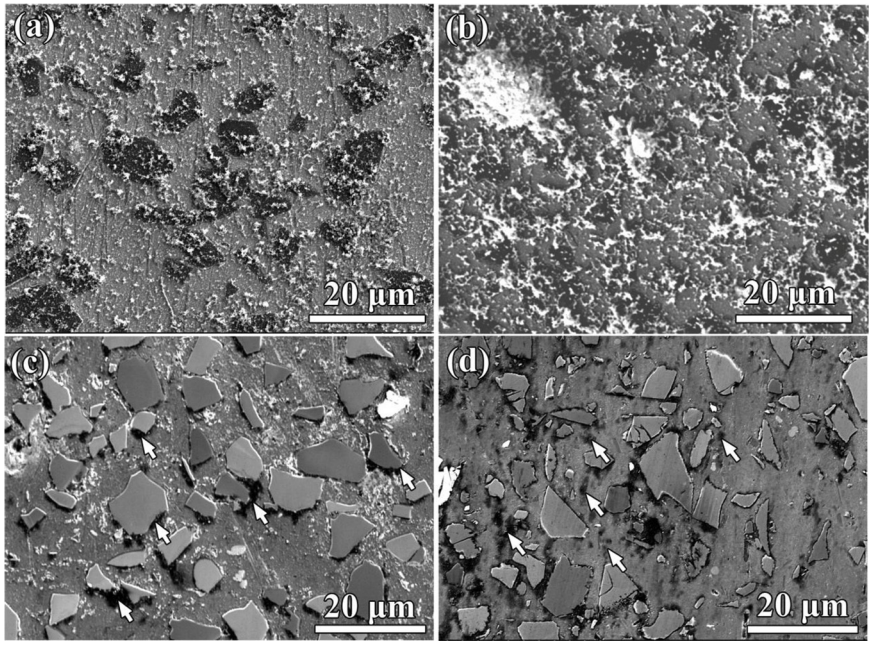

Fig. 6. Characterization of the materials suffered immersion in H_3BO_3 solution for 120 h. (a) and (b) SEM images of the samples HP560 and HP620, respectively. The surfaces are covered by corrosion product sedimentation. (c) and (d) SEM images of the corroded surfaces of the samples HP560 and HP620, respectively, after removing the corrosion products. The corrosion sites are marked by arrows.

Mg_2Si is the main precipitate in the sample HP560. One may take interest in their electrochemical effect on the present composite since their effect on the corrosion of 6xxx series alloys has been widely studied [38–42]. Fig. 9(a) displays a HAADF image of the Mg_2Si particles in the aluminum matrix. Suffered as short as 1 h immersion, the Mg_2Si precipitates showed darker contrast than before (Fig. 9(b)), indicating the composition changes.

Then we performed EDS analysis under STEM mode on an individual Mg_2Si precipitate. Fig. 10(a) and (c) show HAADF images of the precipitate before and after immersion. The EDS profiles shown in Fig. 10(b) and (d) were obtained from the line-scanning along the lines in Fig. 10(a) and (c), respectively. Being distinct with the pristine Mg_2Si precipitate, the later one composed of Si and O. This result is in agreement with Kairy et al.'s quasi in-situ TEM work [31].

After dealloying, the remnant compound became stable. Fig. 11(a) shows a HAADF image of a typical area including a B_4C particle and a Mg_2Si particle with large size (in the lower right corner). After exposure in solution for 3 h (Fig. 11(b)), pitting was found to take place at the B_4C/Al interfaces. However, the Si-rich remnant did not promote further corrosion of the aluminum matrix. It is generally accepted that the

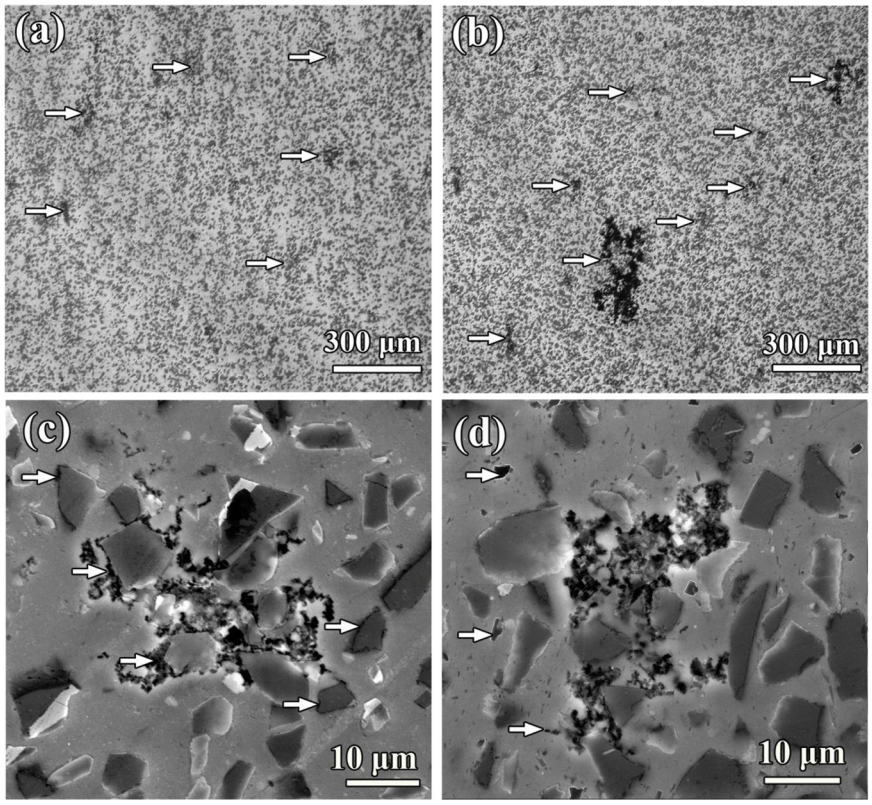

Fig. 7. The corrosion morphologies of the materials after soaking in 600-ppm Cl^--containing H_3BO_3 solution for 24 h. (a) and (b) Optical micrographs of the specimen HP560 and HP620, respectively. The corrosion pits are clearly visible under microscope, as arrowed. The pits on the specimen HP620 are larger and deeper. (c) SEM image of a corrosion site on the HP560. Trenching around the B_4C particles indicates the corrosion initiation there. (d) SEM image of the corroded sample HP620. Besides at the B_4C/Al interfaces, massive corrosion pits are observed on the alloy matrix. Some larger ones are marked by arrows.

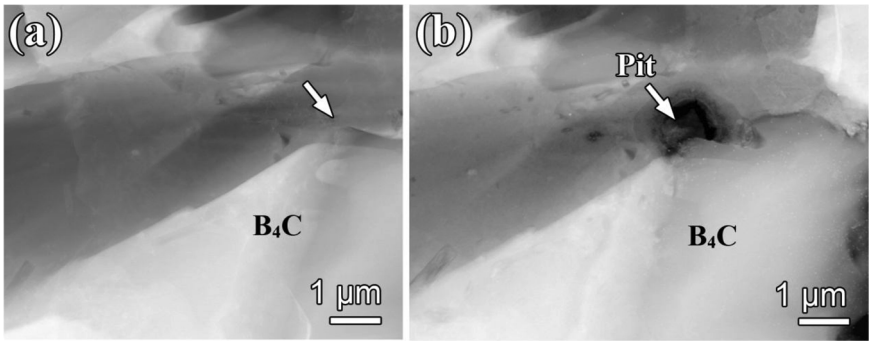

Fig. 8. Quasi in-situ TEM observation of the pitting initiation in the specimen HP560. (a) HAADF image of the B_4C/Al interface. (b) The same place as that in (a) but experienced 2 h immersion in Cl^--containing H_3BO_3 solution. The pit formed at the corner of a notch on the B_4C surface (arrowed).

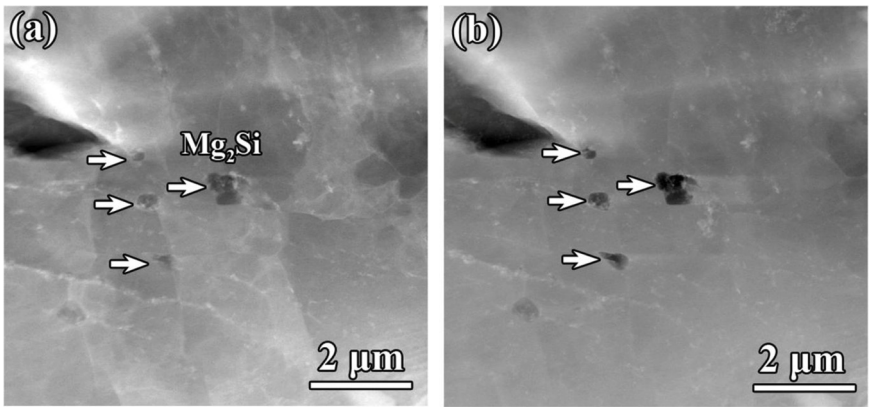

Fig. 9. Quasi in-situ TEM observation of the corrosion response of Mg_2Si precipitates in the sample HP560. (a) HAADF image of the Mg_2Si particles in the alloy matrix. (b) Immersed in Cl^--containing H_3BO_3 solution for 1 h, the Mg_2Si particles displayed in (a) show dark contrast, indicating the composition changes.

corrosion potential of Mg_2Si is lower than Al, leading to the dealloying of the precipitates. Then the Si-rich remnant may turn into a cathode and facilitate pitting occurrence [38,39]. Nevertheless, we failed to confirm the phenomenon by prolonging immersion time of the foils in solution since the corrosion developed very fast once the pitting occurred at the B_4C/Al interfaces and damage the thin areas in a TEM foil.

As a comparison, quasi in-situ TEM observations were carried out on the composite HP620 as well. Pitting at the B_4C/Al interface could also be found. As shown in Fig. 12(a) and (b), a pit is seen between the two neighboring B_4C particles. The lower B_4C particle possesses a sharp corner and the dissolution of aluminum matrix seems to initiate at the corner which was totally exposed in the dissolved pit. The high-magnification bright-field micrographs of the areas framed in Fig. 12(b) are displayed in Fig. 12(c)–(e). As marked by white arrows, Al_3BC particles remain on the B_4C surfaces. The electron diffraction performed on the Al_3BC in Fig. 12(e) is shown in Fig. 12(f). The perfect crystalline characteristic indicates that the compound was unattacked during the corrosion process.

In this sample, we found that the MRR product MgB_2 dispersions in aluminum matrix were an important factor promoting localized corrosion. Fig. 13(a) shows a HAADF image of the alloy matrix where the MgB_2 nano-rods are located. The same place after 2 h immersion in solution is given in Fig. 13(b) in which two small corrosion pits are found at the periphery of the MgB_2 rod, as arrowed. Fig. 14 shows more evidence that the localized corrosion was induced by an individual MgB_2 nano-rod (Fig. 14(a) and (b)) and a bundle of MgB_2 rods (Fig. 14(c) and (d)).

Extending the immersion time to 3 h, we could find the corroded areas expanded and formed narrow trenches, as shown in Fig. 15(a). Inside the two largest dissolved areas, MgB_2 nano-rods as marked by arrows are featured. In other severely dissolved trenches, embedded MgB_2 nano-rods could be easily found as well (see more examples in Fig. 15(b) and (c)). The corrosion trenching is identical with that in the SEM observation in Fig. 7(d).

The compositional and structural characteristics of the MgB_2 nano-rod which gave rise to pitting were further studied. Fig. 16(a) shows a HAADF image and corresponding EDS elemental maps of the MgB_2 nano-rod located in the center of a corrosion trench. The nano-rod is still composed of Mg, Al and B. Moreover, the surfaces of the rod are rich in oxygen and decorated with several copper particles. The bright-field imaging (Fig. 16(b)) and diffraction (Fig. 16(c)) on the nano-rod indicated the compound retained its crystalline structure. Obviously, galvanic cell was formed between the MgB_2 compound and the nearby aluminum matrix. MgB_2 rods served as the cathode in the corrosion process and promoted the dissolution of aluminum continuously taking place.

4. Discussion

Deduced from the sharply increasing anodic current in polarization curves, pitting has occurred on the B_4C/Al composite in H_3BO_3 solution and in Cl^--containing H_3BO_3 solution. According to the corrosion morphologies shown above, a high density of pitting nucleation was found. The presence of Cl^- remarkably increased the corrosion rate and some of pits have developed to a large scale in 24 h, which could be clearly visible under optical microscope. The severe pitting was also confirmed by the anodic current densities in the polarization curves, which is about one order of magnitude higher than that measured in pure boric acid. The slow corrosion rate in H_3BO_3 solution should be partly ascribed to the corrosion product depositions, as shown in Fig. 6(a) and (b). As corrosion progressed, the main corrosion product aluminum hydroxide [14] on the specimen surface acted as a barrier and prevented the contact between metal and electrolyte. In consequence, the propagation of the formed pits was retarded. By contrast,

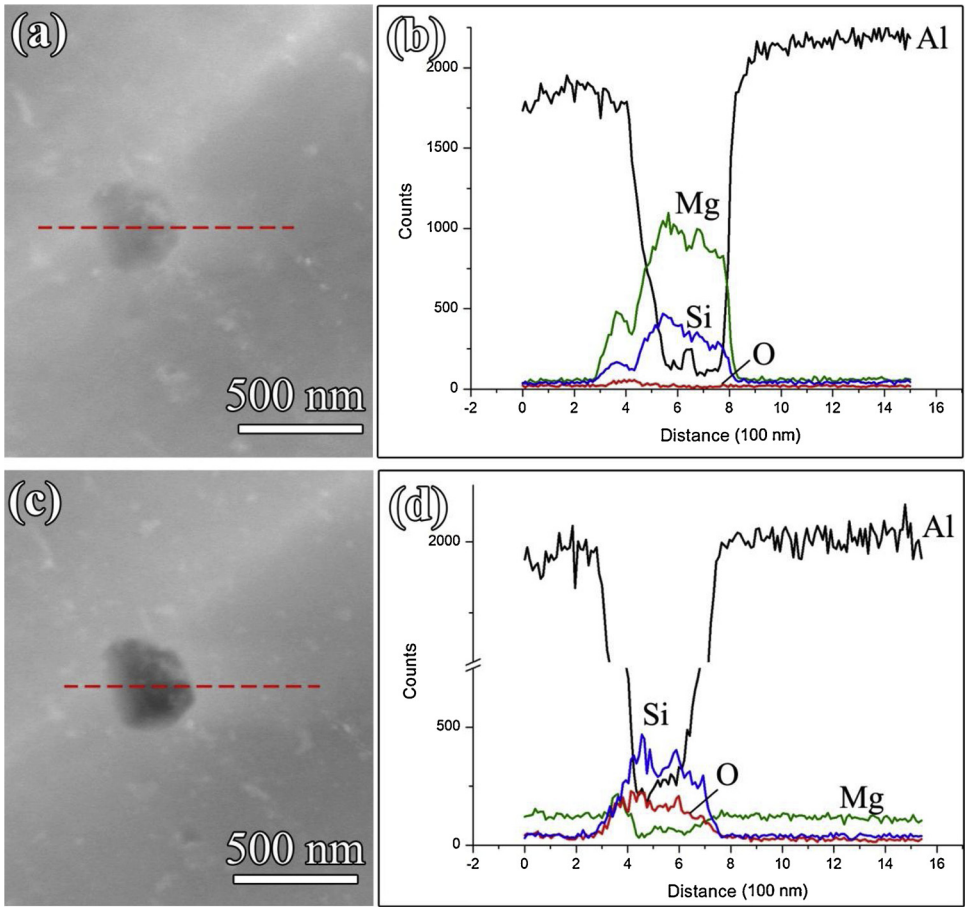

Fig. 10. EDS analysis on a Mg_2Si precipitate. (a) HAADF image of a Mg_2Si particle in the sample HP560. (b) The result of the EDS line profile along the red line in (a). (c) HAADF image of the same Mg_2Si particle shown in (a) but suffered 1 h immersion in solution. (d) EDS line profile of the Mg_2Si remnant showing the depletion of Mg and enrichment of Si and O. (For interpretation of the references to colour in this figure legend, the reader is referred to the web version of this article.)

the Cl^- contamination in H_3BO_3 solution has a remarkably harmful effect, which is in agreement with the previous report [16]. In the environment containing Cl^-, soluble aluminum oxychlorides are expected to generate [43]. Once the pitting initiated, fresh metal matrix would expose to the corrosive electrolyte and stable pits would easily form and propagate, as shown in Fig. 7.

In terms of the microstructures in the composites, the electrochemical effects of the different phases are discussed as follows.

B_4C reinforcement is highly concerned in the composite. B_4C is a semiconductor possessing a noble electrode potential with respect to the aluminum matrix [19,21]. When the semiconducting ceramic particles are introduced into metal matrix, galvanic corrosion will theoretically take place due to the difference in electrode potentials. As suggested by Ding et al. [19], however, the galvanic current in the B_4C-Al system is rather low probably due to the high over-potential for cathodic reactions on B_4C electrode. Therefore, the galvanic coupling between B_4C and aluminum matrix can partly explain the preferential dissolution at the B_4C/Al interface but not the sole reason, especially in the Cl^--containing solution. Instead, we proposed that the debonding (or nonepitaxial bonding) at the interfaces should be considered for the sites being vulnerable to be attacked. The pitting onset at the B_4C/Al boundaries, like the ones in Figs. 8, 11 and 12, were mostly found at the periphery of the sharp corners of B_4C particles. Although we did not observe evident crevices by TEM, it is very likely to form nano-void at these sites where the loading stress tends concentrated during mechanical processing. Therefore, the possible nano-voids or the discontinuity of the protective oxide film at the places would result in the high susceptibility of localized corrosion.

Being distinct with the 'clean' B_4C/Al interface in the sample HP560, the MRR at the B_4C/Al interface in the HP620 generate a semiconductor Al_3BC layer. It obviously increases the complexity of the galvanic system. Firstly, as shown in Fig. 12, the Al_3BC compound in the corrosion pit does not show any degradation, indicating its higher corrosion potential than the aluminum. It possibly acts as a new cathode whose effect depends on its electrode potential and the cathodic reaction kinetics on its surfaces. Secondly, the junction

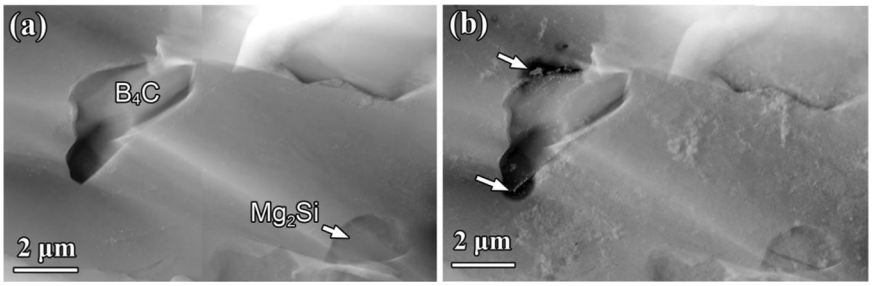

Fig. 11. (a) HAADF image of an area containing B_4C particles and a Mg_2Si precipitate with large size. (b) The same area after 3 h exposure in solution. Two pits formed at periphery of the B_4C particle, but the Mg_2Si remains stable after dealloying.

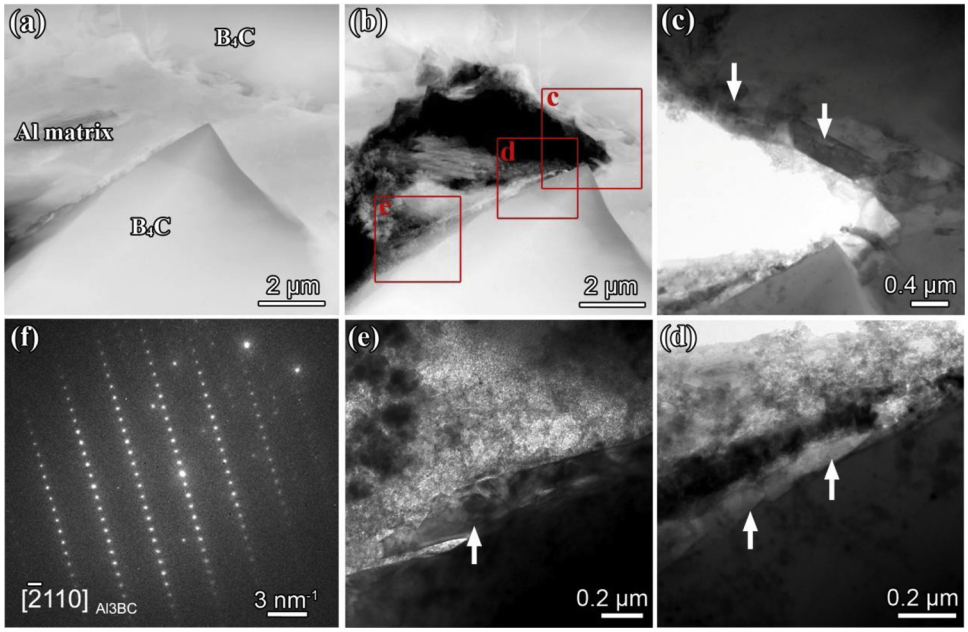

Fig. 12. Quasi in-situ TEM observation of the pitting at the B_4C/Al interface in the sample HP620. (a) and (b) HAADF images of the B_4C/Al interfaces before and after immersion in Cl^--containing H_3BO_3 solution (2 h), respectively. A large pit formed between the neighboring B_4C particles. (c), (d) and (e) High-magnification BF-TEM images of the areas corresponding to the frames in (b). As arrowed, Al_3BC particles are observed. (f) SAED pattern of the Al_3BC particle in (e) showing it did not undergoes corrosion.

barriers at the Al_3BC/Al and B_4C/Al_3BC interfaces should have significant influence on the corrosion current flow running through the electrodes. To the authors' knowledge, however, the physical parameters of Al_3BC compound are unavailable; thus the prediction of its influence on the galvanic couples between B_4C and Al is not easy. On the other hand, the interfacial reaction product is beneficial to the bonding state of the B_4C/Al interface. The stress concentration induced nano-void at the interface can be reduced, which makes the interface more resistant to pitting attack. From this point of view, the presence of Al_3BC is possibly salutary to the composite. According to the corrosion morphology observed in this work, it seems that Al_3BC does not show obvious deterioration to the corrosion resistance.

In contrast, the experimental results unambiguously demonstrate that another MRR product, i.e. MgB_2 nano-rods, increase the corrosion susceptibility of the B_4C-6061Al composite. The cathodic role of MgB_2 is similar to that of AlB_2 as reported by Pohlman [23]. MgB_2 nano-rods are conductive [44] and can effectively facilitate the anodic dissolution of the surrounding Al matrix via galvanic coupling.

On the other hand, if we carefully examine the MgB_2 nano-rods inside the corrosion pits in Figs. 14 and 16(b), it will be found that some of the surface areas of the rods underwent dissolution as well. According to the previous research [45], acid solution can catalyze the decomposition of pure MgB_2 and generate magnesium hydroxide and boron oxide. Therefore, the partial dissolution and surface oxidation of MgB_2 in the composite can be interpreted as: when a pit formed, the pH in the anodic region became lower [20] and the acidification resulted in its decomposition.

In addition, on the MgB_2 nano-rods inside pits, several nanoparticles with bright contrast in HAADF images (e.g. Figs. 15 and 16) were observed. The EDS mapping in Fig. 16(a) suggests that they are copper particles. Copper redeposition was frequently observed in corroded Cu-containing aluminum alloys [31,46,47]. The cupric ions (Cu^{2+}) released from the dissolved alloy are preferentially reduced and deposite on the cathodic sites [47]. At the same time, the copper deposits could act as new cathodes and promote the efficiency of pitting corrosion. The deposition of copper can also be seen at the surfaces of B_4C particles, especially at the exposed surfaces in corrosion pits (see Fig. 11). In turn, this phenomenon confirms that MgB_2 and B_4C both are cathodic sites.

Mg_2Si is a common precipitate in Al-Mg-Si alloys. As usual, Mg_2Si is anodic to the alloy base and the element Mg tends to selectively dissolve when it is exposed to electrolyte. The electrochemical role of the Mg_2Si remnant is under debate [38,39,48,49]. Some authors demonstrated that the Si-rich remnant after dealloying of Mg could transform to cathode, leading to the anodic dissolution and corrosion of the alloy base [38,39]. In our quasi in-situ TEM experiments, we did not find the evidence of pitting occurrence at its adjacent periphery, probably due to the short immersion time when corrosion pits started to form at the B_4C/Al interfaces. However, it also should be noted that the remnant

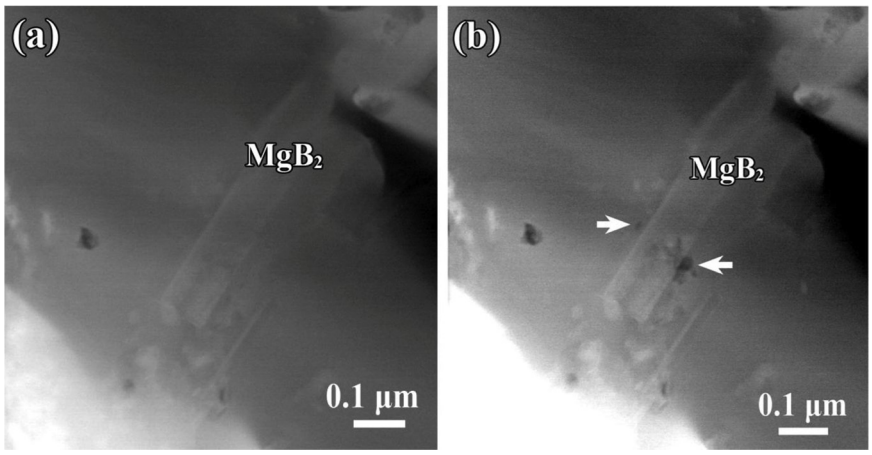

Fig. 13. Quasi in-situ TEM observation indicating the localized corrosion happened at the periphery of MgB_2 nano-rods. (a) HAADF image of the MgB_2 nano-rods in the Al matrix in the sample HP620 (b) HAADF image of the area after 2 h immersion in 600-ppm Cl^--containing H_3BO_3 solution. The dark contrast as marked by arrows indicates the corrosion nucleation.

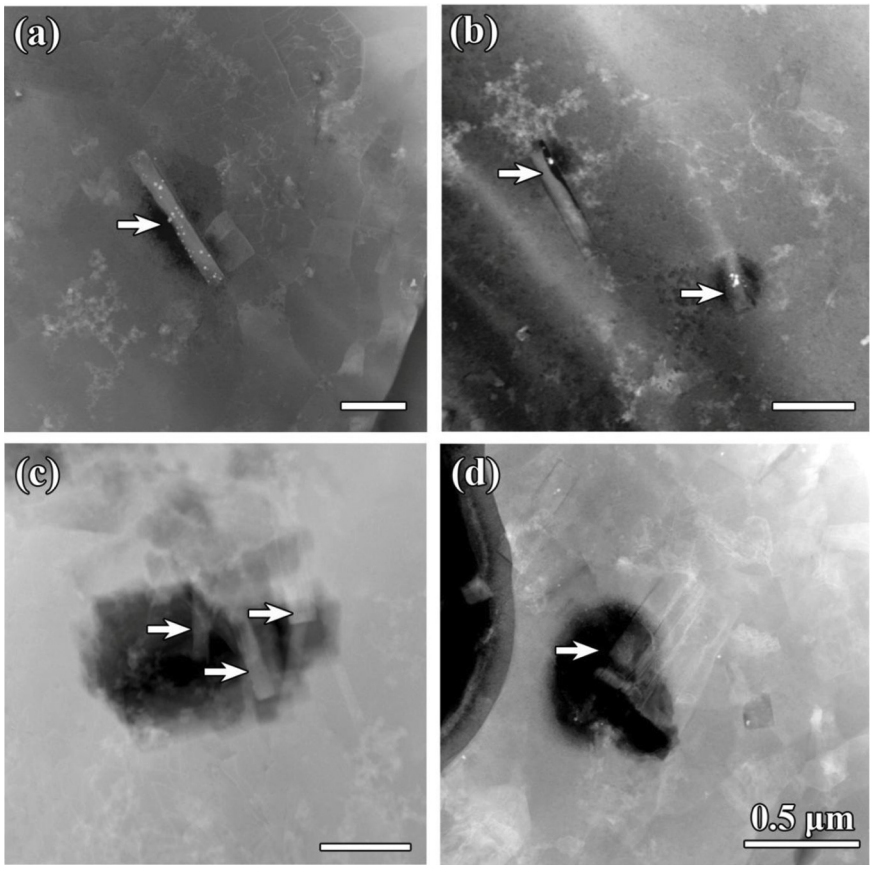

Fig. 14. HAADF images showing more examples of the corrosion initiation at the periphery of MgB_2 nano-rods.

was rich in oxygen (Fig. 10(d)), which was in agreement with Mizuno et al.'s result [49]. Silicon oxide is electrochemically passive and can remarkably suppress the cathodic reactions. Therefore, galvanic effect of the Mg_2Si remnant in the present material should not be very harmful to the corrosion resistance.

5. Conclusions

In the present work, the microstructures and the corrosion behavior of the B_4C-6061Al composites hot-pressed at 560 °C and 620 °C were investigated. Quasi in-situ TEM experiments were carried out to reveal the correlations between corrosion onset and the reinforcement/secondary phases in the samples. The following conclusions can be drawn:

1 In the sample hot-pressed at 560 °C, chemical reaction between the B_4C reinforcement and the alloy matrix is not obvious and Mg_2Si is the main precipitate. When the pressing temperature was increased to 620 °C, B_4C readily reacted with the metal matrix and generated Al_3BC at the interfaces as well as MgB_2 dispersion in the matrix.
2 Potentiodynamic polarization measurements on the samples indicated that the sample HP620 is more susceptible to corrosion attack in H_3BO_3 solution and in Cl^--containing H_3BO_3 solution. Immersion tests proved that B_4C/Al interfaces in the samples HP560 and HP620 are the preferential sites for corrosion occurred. However, the secondary phases in the alloy matrix in HP620 have great influence on the corrosion susceptibility of the material.
3 Quasi in-situ TEM observations confirmed the pitting initiation at the B_4C/Al interface. The existence of Al_3BC at the interfaces does not obviously increase the corrosion sensitivity. The pits at the periphery of the sharp corners of B_4C particles, which were frequently observed in experiments, imply the discontinuity of surface oxide film or the nano-void at the place possibly being an important reason for the high pitting sensitivity in Cl^--containing solutions.
4 Selective dissolution of Mg was observed in Mg_2Si precipitate when

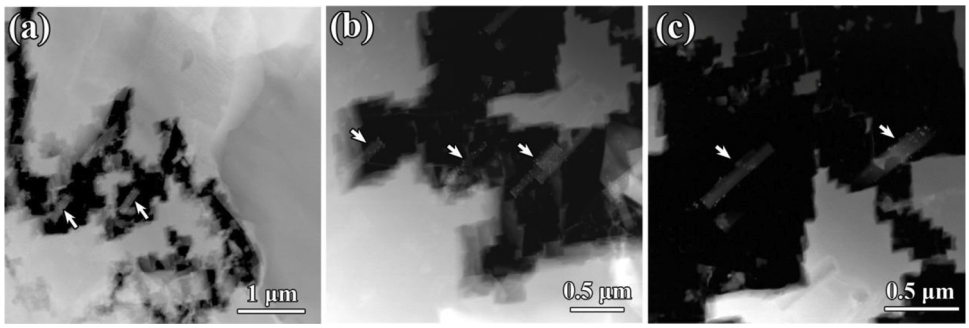

Fig. 15. HAADF images of severely corroded areas. The corrosion trenches expand along grain boundaries. In the crevices, several MgB_2 nano-rods can be found (as arrowed).

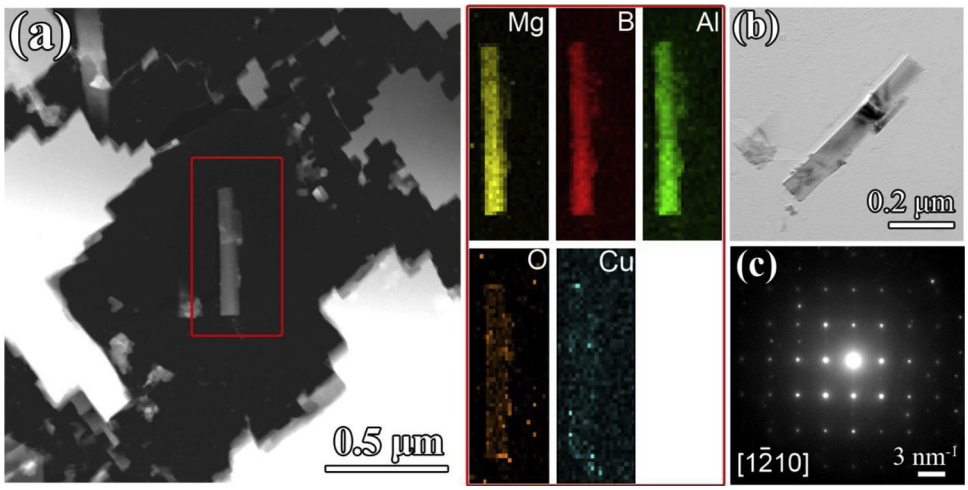

Fig. 16. TEM characterization of the MgB_2 nano-rod inside a corrosion trench. (a) HAADF image and the corresponding EDS elemental maps of the MgB_2 nano-rod. It is still composed of Mg, Al and B. In addition, the surface of the rod is rich in O (oxygen) and decorated by several Cu nanoparticles. (b) BF-TEM image and (c) SAED pattern of the nano-rod indicating that it remains the pristine crystalline structure.

the sample HP560 was exposed to solution. We did not find the evidence that further localized corrosion could be induced by the dealloyed Mg_2Si when severe pitting occurred at the B_4C/Al interfaces. By contrast, the MRR product MgB_2 nano-rods dispersed in the sample HP620 serve as cathodic sites and are detrimental to the corrosion resistance of the material.

Data availability

The raw/processed data required to reproduce these findings cannot be shared at this time, as the data form part of another ongoing study.

Acknowledgements

This work is supported by the National Natural Science Foundation of China (U1508216, 51501195) and Liaoning Province (20180551101), Innovation Fund of IMR (2017-PY10). Mr. B. Wu and L.X. Yang of this laboratory are acknowledged for their technical support on TEM experiments.

References

[1] D.J. Llyod, Particle reinforced aluminium and magnesium matrix composites, Int. Mater. Rev. 39 (1994) 1–23.
[2] A.R. Kennedy, The microstructure and mechanical properties of Al-Si-B_4C metal matrix composites, J. Mater. Sci. 37 (2002) 317–323.
[3] Z. Zhang, T. Topping, Y. Li, R. Vogt, Y. Zhang, C. Haines, J. Paras, D. Kapoor, J.M. Schoenung, E.J. Lavernia, Mechanical behavior of ultrafin-grained Al composites reinforced with B_4C nanoparticles, Scr. Mater. 62 (2011) 652–655.
[4] X.-G. Chen, Application of Al-B_4C metal matrix composites in the nuclear industry for neutron absorber materials, in: N. Gupta, W.H. Hunt (Eds.), Solidification Processing of Metal Matrix Composites, TMS, USA, 2006, pp. 343–350.
[5] X.-G. Chen, L. St-Georges, M. Roux, Mechanical behavior of high boron content Al-B_4C metal matrix composites at elevated temperatures, Mater. Sci. Forum 706–709 (2012) 631–637.
[6] P. Zhang, Y. Li, W. Wang, Z. Gao, B. Wang, The design, fabrication and properties of B_4C/Al neutron absorbers, J. Nucl. Mater. 437 (2013) 350–358.
[7] H.S. Chen, W.X. Wang, Y.L. Li, P. Zhang, H.H. Nie, Q.C. Wu, The design, microstructure and tensile properties of B_4C particulate reinforced 6061Al neutron absorber composites, J. Alloys Compd. 632 (2015) 23–29.
[8] H.S. Chen, W.X. Wang, H.H. Nie, J. Zhou, Y.L. Li, R.F. Liu, Y.Y. Zhang, P. Zhang, Microstructure evolution and mechanical properties of B_4C/6061Al neutron absorber composite sheets fabricated by powder metallurgy, J. Alloys Compd. 730 (2018) 342–351.
[9] H. Chen, W. Wang, H. Nie, J. Zhou, Y. Li, P. Zhang, The dynamic properties of B_4C/6061Al neutron absorber composites fabricated by power metallurgy, Mater. Sci. Technol. 34 (2018) 504–512.
[10] A.V. Pozdniakov, V.S. Zolotorevskiy, R.Yu. Barkov, A. Lotfy, A.I. Bazlov, Microstructure and material characterization of 6063/B_4C and 1545K/B_4C composites produced by two stir casting techniques for nuclear applications, J. Alloys Compd. 664 (2016) 317–320.
[11] J. Shi, C. Shen, L. Zhang, J. Lei, X. Long, X. Zhou, Corrosion mechanism of Al-B_4C composite materials in boric acid, At. Energy Sci. Technol. 46 (2012) 972–977.
[12] V.A. Katkar, G. Gunasekaran, A.G. Rao, P.M. Koli, Effect of the reinforced boron carbide particulate content of AA6061 alloy on formation of the passive film in seawater, Corros. Sci. 53 (2011) 2700–2712.
[13] F. Zhang, J. Brett Wierschke, X. Wang, L. Wang, Nanostructures formation in Al-B_4C neutron absorbing materials after accelerated irradiation and corrosion tests, Microsc. Microanal. 21 (2015) 1159–1160.
[14] Y.-L. Li, W.-X. Wang, H.-S. Chen, J. Zhou, Q.-C. Wu, Corrosion behavior of B_4C/6061Al neutron absorber composite in different H_3BO_3 concentration solutions, Acta Metal. Sin. (Engl. Lett.) 29 (2016) 1037–1046.
[15] Y. Han, D. Gallant, X.G. Chen, Investigation on corrosion behavior of the Al-B_4C metal matrix composite in a mildly oxidizing aqueous environment, Corrosion 67 (2011) 115005-1–115005-11.
[16] Y.M. Han, X.G. Chen, Corrosion characteristics of Al-B_4C metal matrix composites in boric acid solution, Mater. Sci. Forum 877 (2016) 530–536.
[17] Y.M. Han, X.G. Chen, Electrochemical behavior of Al-B_4C metal matrix composites in NaCl solution, Materials 8 (2015) 6455–6470.
[18] Y.-M. Han, D. Gallant, X.G. Chen, Galvanic corrosion associated with Al–B_4C composites/SS304 and Al–B_4C composites/AA6061 couples in NaCl and H_3BO_3 solutions, Electrochim. Acta 94 (2013) 134–142.
[19] H. Ding, L.H. Hihara, Electrochemical behavior of boron carbide and galvanic corrosion of boron carbide reinforced 6092 aluminum composites, ECS Trans. 1 (2006) 103–114.
[20] H. Ding, L.H. Hihara, Localized corrosion currents and pH profile over B_4C, SiC, and Al_2O_3 reinforced 6092 aluminum composites, J. Electrochem. Soc. 152 (2005) B161–B167.
[21] H. Ding, L.H. Hihara, Electrochemical examinations on the corrosion behavior of boron carbide reinforced aluminum-matrix composites, J. Electrochem. Soc. 158 (2011) C118–C124.
[22] L.H. Hihara, Corrosion of aluminium-matrix composites, Corros. Rev. 15 (1997) 361–386.
[23] S.L. Pohlman, Corrosion and electrochemical behaviors of boron aluminum composites, Corrosion 34 (1978) 156–159.
[24] Z. Luo, Y. Song, S. Zhang, D.J. Miller, Interfacial microstructure in a B_4C/Al composite fabricated by pressureless infiltration, Metall. Mater. Trans. A 43 (2011) 281–293.
[25] Y.T. Zhou, Y.N. Zan, S.J. Zheng, Q.Z. Wang, B.L. Xiao, X.L. Ma, Z.Y. Ma, Distribution of the microalloying element Cu in B_4C-reinforced 6061Al composites, J. Alloys Compd. 728 (2017) 112–117.
[26] J. Lai, Z. Zhang, X.G. Chen, Effect of Sc, Zr, and Ti on the interfacial reactions of the B_4C/Al system, J. Mater. Sci. 46 (2010) 451–459.
[27] M. Kubota, Solid-state reaction in mechanically milled and spark plasma sintered Al–B_4C composite materials, J. Alloys Compd. 504 (2010) S319–S322.
[28] F. Toptan, A. Kilicarslan, I. Kerti, The effect of Ti addition on the properties of Al-B_4C interface: a microstructural stud, Mater. Sci. Forum 636–637 (2010) 192–197.
[29] T.D. Burleigh, E. Ludwiczak, R.A. Petri, Intergranular corrosion of an aluminum-magnesium-silicon-copper alloy, Corrosion 51 (1995) 50–55.
[30] S.R.K. Malladi, F.D. Tichelaar, Q. Xu, M.Y. Wu, H. Terryn, J.M.C. Mol, F. Hannour, H.W. Zandbergen, Quasi in-situ analytical TEM to investigate electrochemically induced microstructural changes in alloys: AA2024-T3 as an example, Corros. Sci. 69 (2013).
[31] S.K. Kairy, P.A. Rometsch, C.H.J. Davies, N. Birbilis, On the electrochemical and quasi in-situ corrosion response of the Q-phase ($Al_xCu_yMg_zSi_w$) intermetallic particle in 6xxx series Al-alloys, Corrosion 73 (2017) 87–99.
[32] S.J. Zheng, Y.J. Wang, B. Zhang, Y.L. Zhu, C. Liu, P. Hu, X.L. Ma, Identification of $MnCr_2O_4$ nano-octahedron in catalysing pitting corrosion of austenitic stainless steels, Acta Mater. 58 (2010) 5070–5085.
[33] Y.T. Zhou, Y.J. Wang, S.J. Zheng, B. Zhang, X.L. Ma, Strain-induced preferential dissolution at the dislocation emergences in MnS: an atomic scale study, Philos. Mag. 95 (2015) 2365–2375.
[34] Y.T. Zhou, S.J. Zheng, B. Zhang, X.L. Ma, Atomic scale understanding of the interaction between alloying copper and MnS inclusions in stainless steels in NaCl electrolyte, Corros. Sci. 111 (2016) 414–421.

[35] J. Wang, B. Zhang, Y.T. Zhou, X.L. Ma, Multiple twins of a decagonal approximant embedded in S-Al_2CuMg phase resulting in pitting initiation of a 2024Al alloy, Acta Mater. 82 (2015) 22–31.
[36] S.J. Pennycook, Structure determination through Z-contrast microscopy, Adv. Imag. Electron Phys. 123 (2002) 173–206.
[37] Y.Z. Li, Q.Z. Wang, W.G. Wang, B.L. Xiao, Z.Y. Ma, Interfacial reaction mechanism between matrix and reinforcement in B_4C/6061Al composites, Mater. Chem. Phys. 154 (2015) 107–117.
[38] F. Zeng, Z. Wei, J. Li, C. Li, X. Tan, Z. Zhang, Z. Zheng, Corrosion mechanism associated with Mg_2Si and Si particles in Al–Mg–Si alloys, Trans. Nonferrous Met. Soc. China 21 (2011) 2559–2567.
[39] F. Eckermann, T. Suter, P.J. Uggowitzer, A. Afseth, P. Schmutz, The influence of MgSi particle reactivity and dissolution processes on corrosion in Al–Mg–Si alloys, Electrochim. Acta 54 (2008) 844–855.
[40] R.K. Gupta, N.L. Sukiman, K.M. Fleming, M.A. Gibson, N. Birbilis, Electrochemical behavior and localized corrosion associated with Mg_2Si particles in Al and Mg alloys, ECS Electrochem. Lett. 1 (2012) C1–C3.
[41] S.K. Kairy, P.A. Rometsch, C.H.J. Davies, N. Birbilis, On the intergranular corrosion and hardness evolution of 6xxx series Al-alloys as a function of Si: Mg ratio, Cu content and ageing condition, Corrosion 73 (2017) 1280–1295.
[42] W.J. Liang, P.A. Rometsch, L.F. Cao, N. Birbilis, General aspects related to the corrosion of 6xxx series aluminium alloys: exploring the influence of Mg/Si ratio and Cu, Corros. Sci. 76 (2013) 119–128.
[43] V. Guillaumin, G. Mankowski, Localized corrosion of 6056 T6 aluminium alloy in chloride media, Corros. Sci. 42 (2000) 105–125.
[44] K.D. Belashchenko, M. van Schilfgaarde, V.P. Antropov, Coexistence of covalent and metallic bonding in the boron intercalation superconductor MgB_2, Phys. Rev. B 64 (2001) 092503.
[45] H. Zhu, S. Wang, Z. Li, X. Liu, L. Jiang, Degradation behavior of MgB_2 powders in different medium environment, Mater. Sci. Forum 650 (2010) 172–177.
[46] H.M. Obispo, L.E. Murr, R.M. Arrowood, E.A. Trillo, Copper deposition during the corrosion of aluminum alloy 2024 in sodium chloride solutions, J. Mater. Sci. 35 (2000) 3479–3495.
[47] G.S. Chen, M. Gao, R.P. Wei, Microconstituent-induced pitting corrosion in aluminum alloy 2024-T3, Corrosion 52 (1996) 8–15.
[48] F. Eckermann, T. Suter, P.J. Uggowitzer, A. Afseth, M. Stampanoni, F. Marone, P. Schmutz, In Situ microtomographically monitored and electrochemically controlled corrosion initiation and propagation in AlMgSi alloy AA6016, J. Electrochem. Soc. 156 (2009) C1–C7.
[49] K. Mizuno, A. Nylund, I. Olefjord, Surface reactions during pickling of an aluminium-magnesium-silicon alloy in phosphoric acid, Corros. Sci. 43 (2001) 381–396.